Force generation of KIF1C is impaired by pathogenic mutations

Nida Siddiqui[1,3], Daniel Roth[1], Algirdas Toleikis[1,4], Alexander J. Zwetsloot[1,2], Robert A. Cross[1], and Anne Straube[1,#]

[1] Centre for Mechanochemical Cell Biology & Division of Biomedical Sciences, Warwick Medical School, University of Warwick, Coventry, CV4 7AL, UK

[2] MRC-DTP in Interdisciplinary Biomedical Research, Warwick Medical School, Coventry, CV4 7AL, UK

[3] Current address: AstraZeneca, Granta Park, Cambridge, CB21 6GH, UK

[4] Current address: Vilnius University, Life Sciences Center, 7 Saulėtekio Ave, 10257 Vilnius, Lithuania

[#] correspondence to anne@mechanochemistry.org; +44 (0) 2476 151 169

Abstract

Intracellular transport is essential for neuronal function and survival. The fastest neuronal transporter is the kinesin-3 KIF1C. Mutations in KIF1C cause hereditary spastic paraplegia and cerebellar dysfunction in human patients. However, neither the force generation of the KIF1C motor protein, nor the biophysical and functional properties of pathogenic mutant proteins have been studied thus far.

Here we show that full length KIF1C is a processive motor that can generate forces up to 5.7 pN. We find that KIF1C single molecule processivity relies on its ability to slip and re-engage under load and that its slightly reduced stall force compared to kinesin-1 relates to its enhanced probability to backslip. Two pathogenic mutations P176L and R169W that cause hereditary spastic paraplegia in humans maintain fast, processive single molecule motility in vitro, but with decreased run length and slightly increased unloaded velocity compared to the wildtype motor. Under load in an optical trap, force generation by these mutants is severely reduced. In cells, the same mutants are impaired in producing sufficient force to efficiently relocate organelles.

Our results establish a baseline for the single molecule mechanics of Kif1C and explain how pathogenic mutations at the microtubule-binding interface of KIF1C impair the cellular function of these long-distance transporters and result in neuronal disease.

Introduction

Intracellular transport along microtubules allows the distribution of membrane organelles, and shuttling building blocks and signalling molecules between the nucleus and the cell periphery. The transport is mediated my molecular motor proteins, dynein and kinesins that hydrolyse ATP to step unidirectionally along microtubules. While dynein is the major minus end-directed transporter, more than 20 mammalian kinesins mediate plus-end directed transport (Paschal and Vallee, 1987, Lipka et al., 2016) These translocating kinesins share a conserved N-terminal motor domain of about 350 amino acid length that binds to microtubules and ATP. ATP hydrolysis and microtubule binding affinity are tightly coupled so that kinesins hydrolyse one ATP for each 8nm step along the microtubule (Svoboda et al., 1993, Coy et al., 1999). The stalk and tail of translocating kinesins are diverse and mediate cargo specificity and the regulate motor activity through inhibitory intramolecular interactions (Friedman and Vale, 1999, Kaan et al., 2011, Yamada et al., 2007, Siddiqui et al., 2019).

Perturbed intracellular transport results in neurodegenerative disorders. For example, mutations in three kinesins have been implicated in causing hereditary spastic paraplegia (HSP) and spastic ataxias: KIF5A (SPG10), KIF1A (SPG30) and KIF1C (SPG58) (Reid et al., 2002, Bouslam et al., 2007, Klebe et al., 2012, Gabrych et al., 2019). These disorders present with progressive lower limb spasticity and gait difficulties due to the degeneration of motor neurons in the corticospinal tract (Schule et al., 2016, Hedera et al., 2005, Novarino et al., 2014). Complicated forms of HSP, such as those caused by KIF1C loss of function mutations, present with additional neurological defects such as cerebellar dysfunction, dystonic tremor and demyelinating neuropathy (Marchionni et al., 2019, Dor et al., 2014, Caballero Oteyza et al., 2014, Yucel-Yilmaz et al., 2018). The disease-causing mutations are either located within the KIF1C motor domain and predicted to modify either microtubule binding or nucleotide hydrolysis or result in truncations or instability of the protein through missense mutations (Gabrych et al., 2019, Dor et al., 2014, Caballero Oteyza et al., 2014, Yucel-Yilmaz et al., 2018). Heterozygote mutations usually present with a subclinical phenotype, thus homozygosity or a combination of two different mutations is required for full presentation of SPG58. For example, carriers of KIF1C$_{G102A}$, which modifies the highly conserved nucleotide binding p-loop, and KIF1C$_{P176L}$, which is predicted to modify microtubule binding, present with early onset disease (Caballero Oteyza et al., 2014). Expression in COS-7 African green monkey cells revealed that KIF1C$_{G102A}$ mislocalised to the perinuclear region as opposed to the normal accumulation at the cell periphery, supporting the idea that the mutation perturbs motility. KIF1C$_{P176L}$ localized correctly, but while co-expression of wildtype KIF1C could rescue the perinuclear mislocalization of KIF1C$_{G102A}$, KIF1C$_{P176L}$ could not (Caballero Oteyza et al., 2014). This led to the hypothesis that P176L results in a weakened KIF1C motor. A mutation in a nearby residue, R169W, was identified as a homozygotic mutation in patients with

74 childhood onset cerebellar ataxia (Dor et al., 2014) for which any functional studies are lacking
75 to date.
76 The kinesin-3 KIF1C is a ubiquitously expressed transporter responsible for Golgi to ER
77 trafficking and maintenance of Golgi structure, the delivery of integrins, which is important for
78 cell polarity and adhesion, and the transport of secretory vesicles in neurons (Dorner et al.,
79 1998, Lee et al., 2015, Theisen et al., 2012, Schlager et al., 2010). KIF1C is highly processive,
80 can equally efficiently transport cargo into axons and dendrites and is the most efficient plus
81 end-directed translocator (Lipka et al., 2016, Siddiqui et al., 2019). In contrast to other kinesin-
82 3s, KIF1C is a stable dimer whose autoinhibition is controlled by an intramolecular interaction
83 of its stalk domain with the microtubule binding interface of the motor domain. Upon binding
84 of pseudophosphatase PTPN21 or cargo adapter Hook3 to the stalk, the motor domain is
85 released and can engage with microtubules (Siddiqui et al., 2019). Hook3 can simultaneously
86 interact with KIF1C and dynein to form opposite polarity motor complexes (Kendrick et al.,
87 2019), which might explain why depletion of KIF1C causes a reduction in both anterograde
88 and retrograde transport (Theisen et al., 2012, Siddiqui et al., 2019).
89 Kinesin-3 motors are thought to be weak motors that work in teams for cargo transport (Okada
90 et al., 1995, Okada et al., 2003, Rogers et al., 2001, Nangaku et al., 1994). Under single
91 molecule conditions, Unc104 and KIF1A, the founding members of the kinesin-3 family, are
92 monomeric and move by biased Brownian motion (Okada and Hirokawa, 1999). This
93 generated force of up to 0.15 pN for each monomeric motor (Okada et al., 2003). However,
94 adding a leucine zipper motif to either truncated or full length Unc104 or KIF1A renders the
95 motor into fast and processive kinesins, which can generate forces of about 3 pN (Budaitis et
96 al., 2021, Tomishige et al., 2002). Because KIF1C is a stable dimer, we hypothesised that
97 single molecules of native KIF1C can generate substantial forces.
98 Here we determine the force-generating properties of KIF1C and probe the effects of two
99 pathogenic mutations on single molecule motility, force generation and intracellular transport.
100 We find that full-length recombinant KIF1C has a stall force of 5.7 pN and an average
101 detachment force of 3 pN. While HSP-causing mutations P176L and R169W permit fast and
102 processive unloaded motility, force generation is severely reduced with peak forces of 1.3 pN
103 and 0.7 pN respectively. Even though motors can work in teams inside cells, the weakened
104 motors still show significant intracellular transport defects.
105
106 **Results**
107
108 **KIF1C is a strong, processive motor**
109 To determine the force output of KIF1C, we used a classic single bead optical tweezer assay
110 (Block et al., 1990, Carter and Cross, 2005) to probe the force response of full-length

111 recombinant human KIF1C (Siddiqui et al., 2019) and for comparison full-length *Drosophila*
112 *melanogaster* kinesin heavy chain (KHC) (Coy et al., 1999, Toleikis et al., 2020). In this assay,
113 a single motor protein pulls the bead against the force of the trap until it reaches stall force or
114 detaches. The bead displacement is tracked with nanometer accuracy and forces calculated
115 according to Hooke's law. As expected, KIF1C takes forwards steps of approximately 8 nm
116 length consistent with a kinesin binding site on each tubulin dimer (Figure S1A-B). Both motors
117 produced forces of similar magnitude and duration, although KIF1C force events were more
118 frequently interrupted by backwards slippage events (Figure 1A). KHC backslips once for
119 every 6.3 forward steps and manages to stop backslips at the next binding site in the vast
120 majority of cases, while Kif1C backslips double as frequently and three times as many KIF1C
121 backslips are larger than 12 nm, suggesting that KIF1C is both more likely to slip backwards
122 and to slip further when it does so (KHC: 13% of backslips >12nm; KIF1C 38% of backslips
123 >12nm) (Figure 1B). As the ratio of detachments to forward steps is also higher in KIF1C, the
124 average duration of KIF1C force events is reduced by 35% compared to KHC (KHC 1.23 ±
125 0.09 and KIF1C 0.80 ± 0.02, mean ± SEM) (Figure 1C). Under the conditions of our assay,
126 the stall force of KHC, i.e. the force at which the probability of taking a forwards step or slipping
127 backwards is equal, was 7.3 ± 0.2 pN (mean ± SD), while the average detachment force was
128 4.1 ± 0.07 (mean ± SEM) pN (Figure 1D-E). These values are in agreement with published
129 literature (Khalil et al., 2008, Carter and Cross, 2005, Budaitis et al., 2021, Svoboda et al.,
130 1993, Yildiz et al., 2008, Ray et al., 1993). KIF1C generated slightly lower force and stalled at
131 5.7 ± 0.2 pN (mean ± SD), and its average detachment force was 3.0 ± 0.04 pN (mean ± SEM)
132 (Figure 1D-E). For comparison, the detachment forces of constitutively active truncated KIF1A
133 and Unc104 were reported as 2.7 and 2.4 pN, respectively (Budaitis et al., 2021), while native
134 KIF1A is only weakly processive with a stall force of 0.15 pN (Okada et al., 2003). Free-running
135 beads with a single KIF1C move at about 1 µm/s, but its average forward speed decreases
136 under the load of the trap and reaches zero at 7pN. In comparison, KHC can maintain an
137 average speed of 450 nm/s under force of up to 2.5 pN before slowing down rapidly and
138 forward speed is zero at its stall force (Figure 1F, Figure S1C).
139 Thus KIF1C is not only a highly processive motor (Siddiqui et al., 2019), but also generates
140 substantial forces, which might explain why KIF1C translocates cargoes in cells more
141 efficiently than any other kinesin (Lipka et al., 2016).
142
143 **Pathogenic mutations increase off rate and speed of KIF1C**
144 In recent years, disease-causing mutations have been identified for a number of patients
145 representing with complicated forms of hereditary spastic paraplegia or spastic ataxias. Two
146 of these, P176L (Caballero Oteyza et al., 2014) and R169W (Dor et al., 2014) are located in
147 the motor domain of KIF1C close to the microtubule binding interface (Figure 2A), but how

148 these affect the biophysical properties of KIF1C is currently unclear. Thus, we introduced both
149 mutations and purified full-length recombinant human KIF1C-GFP with each mutation from
150 insect cells (Figure 2B). To investigate the effect of these pathogenic mutations, we first
151 determined in single molecule assays whether the motors can still bind and move along
152 microtubules. Both KIF1C patient mutant proteins, KIF1C$_{P176L}$-GFP and KIF1C$_{R169W}$-GFP were
153 motile in the single molecule motility assays and showed microtubule plus-end accumulation
154 similarly to the wildtype (Figure 2C), suggesting that the mutants are still able to move
155 processively along microtubules. Under the conditions of the assay, we observe slightly more
156 than half of motors being static or moving very slowly (< 25 nm/s). The fraction of static motors
157 was slightly increased for both mutants (wt: 53 ± 5 %; P176L: 65 ± 9 %; R169W: 61 ± 7 %
158 (mean ± SD)). Diffusing motors are observed occasionally for wildtype KIF1C, but were
159 increased more than two-fold for the mutants (wt: 3.9 ± 3.9 %; P176L: 8.2 ± 3.4 %; R169W:
160 8.6 ± 4.5 % (mean ± SD)). Taken together, this resulted in a ~30% reduction in motile motors
161 (wt: 43 ± 6 %; P176L: 27 ± 6 %; R169W: 30 ± 10 % (mean ± SD)) (Figure 2D-E). Detailed
162 analysis of single molecule motility revealed that the dwell time of both mutants was
163 significantly reduced (wt: 36.3 ± 1.4 s; P176L: 25.8 ± 1.6 s; R169W: 16.0 ± 1.3 s (mean ±
164 SEM)) (Figure 2F). As both mutations are located at the microtubule binding interface of
165 KIF1C, the increase in diffusive events and faster off rates suggest that microtubule binding
166 of both mutants is reduced. Even though the speed was increased (wt: 284 ± 15 nm/s; P176L:
167 319 ± 29 nm/s; R169W: 362 ± 24 nm/s (mean ± SEM)) (Figure 2G), the fast off rate resulted
168 in significantly shorter run length of both mutants compared to wild type KIF1C (wt: 5.08 ±
169 0.19 µm; P176L: 3.44 ± 0.15 µm; R169W: 2.80 ± 0.18 µm (mean ± SEM)) (Figure 2H). KIF1C
170 motors frequently pause during runs (Figure 2D), the duration of run phases was more strongly
171 reduced (-24% for P176L and -58% for R169W compared to wt) as a result of the mutations
172 than the duration of pauses (not significantly changed for P176L and -32% for R169W
173 compared to wt) (Figure S2), suggesting that motors are more prone to detachment during
174 runs. Thus, our single molecule analysis of full length KIF1C wildtype and P176L and R169W
175 mutants suggests that both pathogenic mutations reduce microtubule binding affinity, which
176 results in faster motility, but a higher off rate and shorter run length.
177
178 **Pathogenic KIF1C mutants are impaired in force generation**
179 In cells, motors haul cargoes against the viscous drag of the cytoplasm and various
180 intracellular structures. Thus, to understand how the reduced microtubule affinity affects the
181 ability to step under load, we analysed both KIF1C$_{P176L}$-GFP and KIF1C$_{R169W}$-GFP using the
182 optical trap. At the trap stiffness we used to analyse KIF1C wild type motors (Figure 1), we did
183 not observe significant bead displacements for the mutants. To confirm that motors were
184 present on the beads, we positioned beads on the microtubule and then switched the trap off

185 to let the motor run without load. This confirmed the presence of functional motors (Figure
186 3A), but these were too weak to generate forces comparable to the wildtype motor. We then
187 collected bead displacement data at reduced trap stiffness (see methods for details) and
188 detected short runs for KIF1C$_{P176L}$-GFP with an average peak force of 1.3 ± 0.03 pN (mean ±
189 SEM), compared to 3.5 ± 0.03 pN (mean ± SEM) for the wildtype motor (Figure 3B-C).
190 KIF1C$_{R169W}$-GFP moved the bead only small distances when the trap was switched off and
191 could not generate forces above 1 pN (Figure 3B-C). These data suggest that the moderate
192 reduction in processivity of unloaded motors observed in single molecule assays are
193 exacerbated once the motors have to generate forces against a load.
194
195 **Pathogenic mutations impair cellular cargo transport**
196 In cells, motors could work in teams and thereby might be able to compensate for the reduction
197 in force generation on the single molecule level. In order to test this, we first analysed the
198 ability of KIF1C with the pathogenic mutations to localise to the cell periphery, which would
199 indicate that they are able to move through the cytoplasm, presumably while carrying cargoes.
200 KIF1C-GFP accumulates in the tails of migrating RPE1 cells as previously reported (Theisen
201 et al., 2012, Siddiqui et al., 2019). As the extent of the tail accumulation depends on whether
202 the tail is currently growing, stable or retracting (Theisen et al., 2012), we used KIF1C-mCherry
203 as a marker for tail status and co-expressed KIF1C-GFP, KIF1C$_{P176L}$-GFP and KIF1C$_{R169W}$-
204 GFP in RPE1 cells to test their ability to localise to the cell tail. Even though endogenous and
205 wildtype KIF1C-mCherry were present and might allow for heterodimerisation with the
206 mutants, we found that tail accumulation of KIF1C$_{R169W}$-GFP (1.02 ± 0.03 (mean ± SEM)); was
207 significantly reduced compared to wildtype KIF1C-GFP (1.43 ± 0.04 (mean ± SEM)).
208 Surprisingly, KIF1C$_{P176L}$-GFP accumulated stronger in tail tips (1.66 ± 0.05 (mean ± SEM))
209 than the wildtype (Figure 4A-B). One possible explanation could be that the P176L mutation
210 weakens the autoinhibitory interaction between stalk and motor domain as a stalk deletion
211 mutant also over-accumulated in cell tips (Siddiqui et al., 2019). However, we didn't detect a
212 significant increase in KIF1C$_{P176L}$-GFP landing rate in our *in vitro* experiments, which is
213 inconsistent with the idea of hyperactivation. An alternative explanation is that KIF1C$_{P176L}$-GFP
214 is not arriving at a higher rate at cell tips, but is retained more strongly or fails to efficiently
215 participate in retrograde transport.
216 To more directly test force generation in cells, we recruited wildtype and mutated motors to
217 mitochondria as a relatively large organelle that would be expected to generate a significant
218 amount of viscous drag in the cytoplasm, but also allow large teams of motors to work
219 together. To do this, we co-expressed FKBP-GFP-myc-MAO with either KIF1C-mCherry-FRB,
220 KIF1C$_{P176L}$-mCherry-FRB or KIF1C$_{R169W}$-mCherry-FRB. The tagged monoamine oxidase
221 allowed us to visualise normal mitochondria morphology and distribution before recruiting the

222 full-length motors to the outer mitochondria membrane. Recruitment of wildtype KIF1C caused
223 dramatic changes in mitochondria morphology within seconds of adding rapamycin. The
224 pulling forces fragmented mitochondria into thin outer membrane tubules and beads (Figure
225 4C). Both tubules and beads were transported towards the cell edges efficiently, resulting in
226 a near complete accumulation of mitochondria to the cell tips within the 20 minutes of the
227 experiment (Figure 4D-E). KIF1C$_{P176L}$-mCherry-FRB caused the same mitochondria beading
228 effect albeit more slowly and transported mitochondria to the cell periphery less efficiently than
229 the wildtype motor (Figure 4D-E). KIF1C$_{R169W}$-mCherry-FRB was recruited very efficiently to
230 mitochondria membranes and accumulated on the periphery facing tip of the membrane.
231 Beading was only observed in cells expressing a relatively large amount of KIF1C$_{R169W}$ and
232 then the motor was unable to efficiently move the large (700-1000 nm diameter) cargo. In
233 most cases, normal tubular mitochondria morphology was retained and a subset of these was
234 transported towards the cell periphery (Figure 4D-E). At the beginning of the experiment, the
235 fluorescence signal for the mitochondria marker near the cell periphery was about 25% lower
236 than in the perinuclear area and equal between all three conditions (Figure 4F). Immediately
237 after adding rapamycin, the signal shifted towards the periphery, albeit at a significantly higher
238 rate in cells expressing wildtype KIF1C-mCherry-FRB or KIF1C$_{P176L}$-mCherry-FRB than the
239 R169W mutant. 20 minutes after adding rapamycin, the ratio of peripheral versus centrally
240 located mitochondria was clearly lower compared to wildtype KIF1C (Figure 4F) (wt: 1.58 ±
241 0.09; P176L: 1.31 ± 0.05, p=0.01; R169W: 0.94 ± 0.04, $p=3 \cdot 10^{-11}$ (mean ± SEM, t-tests with
242 Bonferroni correction)). Analysing the KIF1C distribution at the start of the experiment showed
243 a large cytoplasmic pool and strongly reduced tail accumulation of KIF1C$_{R169W}$-mCherry-FRB
244 and the overaccumulation of KIF1C$_{P176L}$-mCherry-FRB in cells tips (Figure 4G). The
245 discrepancy between KIF1C accumulation in tips versus ability to redistribute mitochondria
246 suggests that even if motors with pathogenic mutations cooperate, they cannot compensate
247 for their reduced force generation abilities.
248
249 **Discussion**
250 KIF1C is a highly efficient transporter in cells. Here we describe for the first time its force
251 generating properties. We find that a single KIF1C molecule takes processive ~8nm steps
252 against the force of the optical trap, stalls at 5.7 pN and detaches at 3 pN on average. Thus
253 KIF1C's force output is about 25% lower than that of conventional kinesin, but dramatically
254 higher than the < 1 pN detachment forces observed for full length KIF1A and slightly higher
255 than that measured for a constitutively active KIF1A mutant (Budaitis et al., 2021). While we
256 observe a ~2-fold higher probability of backward slipping for KIF1C, force-generating events
257 are broadly similar to those of conventional kinesin and distinctly different from the 50-fold
258 enhanced slipping observed for constitutively active KIF1A (Budaitis et al., 2021, Lam et al.,

259 2021). We proposed recently that backslips arise when phosphate is released before a
260 forward step is completed, which converts the motor into a weakly bound state that is pulled
261 backwards under the load of the trap. Backwards slipping is stopped when either of the two
262 motor domains in ADP state re-engages at a binding site and releases nucleotide to start
263 another cycle of trying to make a forward step (Toleikis et al., 2020). Kinesin-3s are about
264 tenfold more processive and twice as fast as kinesin-1 (Soppina et al., 2014, Scarabelli et al.,
265 2015). The observations that KIF1C and KIF1A undertake backslips more frequently, suggests
266 that they release phosphate faster, which might be a trade-off for being faster motors.
267 However, due to their interaction with microtubules being significantly stronger (Scarabelli et
268 al., 2015), kinesin-3s stay attached to the microtubule even in a weekly bound state for long
269 enough to wait for the next step.
270 The two pathogenic mutations in the L8 region of KIF1C retain motility of the motor but with
271 reduced run length in line with findings for pathogenic mutations in the microtubule binding
272 interface of KIF1A (Lam et al., 2021, Boyle et al., 2021). However, we find that the unloaded
273 velocity of the motors was not negatively affected and even slightly increased, while mutations
274 in the microtubule binding interface of KIF1A resulted in lower single molecule velocities (Lam
275 et al., 2021, Boyle et al., 2021). This could be due to differences in the mutation sites as
276 S274L, P305L and R316W locate around the kinesin-3 specific K-loop region in α4, 3_{10} helix
277 and α5, while the mutations we studied here are at the β-tubulin facing tip of the motor domain
278 in loop 8. When two L8 mutations (R167S and H171D) were simultaneously introduced into
279 KIF1A, run length was 10-fold and speed two-fold reduced (Scarabelli et al., 2015). Two
280 mutations, E220A and L317A, with slightly higher velocity, but reduced microtubule affinity
281 were identified by alanine scanning mutagenesis in kinesin-1, which did not include the sites
282 studied here (Woehlke et al., 1997). Alternatively, this could be a consequence of the distinct
283 biophysical properties of KIF1A and KIF1C motors. This notion is supported by the observation
284 that KIF1C velocity increases with increasing salt concentration in the assay buffer (data not
285 shown), which presumably reduces microtubule affinity in a similar way as the mutants.
286 Despite retaining processive motility and being able to still reach the plus end of microtubules,
287 the force generation of P176L and R169W mutants was reduced to 1/3 and 1/5 of the wildtype
288 motor, respectively. This demonstrates that these pathogenic KIF1C mutations affect force
289 generation much more dramatically than their unloaded motility. This seems not to be the case
290 for the recently characterised P305L mutation in the 3_{10} helix of KIF1A, which showed a
291 roughly 5-fold reduction in landing rate, a 2-fold reduction in speed and run length and a 2-
292 fold reduction in force generation (Lam et al., 2021). It will require detailed analysis of
293 mutations in different regions of the microtubule binding interface to understand whether these
294 differences are due to a specific function of L8 in limiting the velocity and enhancing force

295 generation of KIF1C or whether the relationship of microtubule affinity and force generation
296 differs between motors from the kinesin-3 family.
297 Ultimately, it will be important to correlate the biophysical properties of the mutated motors
298 with specific defects in neuronal cargo delivery and organelle distribution, defects in neuronal
299 function and survival, time of onset and the severity of the disease presentation in the patients.
300 This would lead to detailed understanding of the disease aetiology and offer a starting point
301 to develop treatment strategies that delay or indeed reverse the symptoms.
302

303 **Materials and methods**

304 **Protein expression and purification**

305 pFastBac-M13-6His-KIF1C-GFP was described previously (Siddiqui et al., 2019) and is
306 available from Addgene (130975). The human patient mutations P176L (Caballero Oteyza et
307 al., 2014) and R169W (Dor et al., 2014) were introduced into this plasmid as follows.
308 *pFastBac-M13-KIF1CGFP*$_{P176L}$ was generated using *pFastBac-M13-6His-KIF1C-GFP* as
309 template in a three-step mutagenesis PCR with upstream primer pFB5' (5'-
310 GATTACGATATCCCAACGACC-3'), downstream primer AS358 (5'-
311 GAAGGGATCCACAGTTCCCCCATCCTC-3') and mutagenesis primer AS528 (5'-
312 CTGCACGTAC**A**GGCCCAGGATG-3'). The fragment containing the mutation was replaced
313 in *pFastBac-M13-6His-KIF1C-GFP* using *Asc*I and *Stu*I. *pFastBac-M13-6His-KIF1C-GFP*$_{R169W}$
314 was generated similarly using upstream primer pFB5', downstream primer UT170 (5'-
315 ACTGACCTTCTCCGAGTCC-3') and mutagenesis primer AS376 (5'-
316 CTGCGGGTC**T**GGGAGCACC-3'). The fragment containing the mutation was replaced in
317 *pFastBac-M13-6His-KIF1C-GFP* using *Asc*I and *Bsi*WI.
318 Purification of full length human KIF1C in insect cells was performed as described previously
319 (Siddiqui et al., 2019). Briefly, pFastBac-M13-6His-KIF1C-GFP, pFastBac-M13-6His-
320 KIF1C$_{P176L}$-GFP, and pFastBac-M13-6His-KIF1C$_{R169W}$-GFP plasmids were transformed into
321 DH10BacYFP competent cells (Trowitzsch et al., 2010) and plated on LB-Agar supplemented
322 with 30 µg/ml kanamycin (#K4000, Sigma), 7 µg/ml gentamycin (#G1372, Sigma), 10 µg/ml
323 tetracycline (#T3258, Sigma, 40 µg/ml Isopropyl β-D-1- thiogalactopyranoside (IPTG,
324 #MB1008, Melford) and 100 µg/ml X-Gal (#MB1001, Melford). Positive transformants (white
325 colonies) were screened by PCR using M13 forward and reverse primers for the integration
326 into the viral genome. The bacmid DNA was isolated from the positive transformants by the
327 alkaline lysis method and transfected into SF9 cells (Invitrogen) with Escort IV (#L-3287,
328 Sigma) according to the manufacturer's protocol. After 5–7 days, the virus (passage 1, P1)
329 was harvested by centrifugation at 300 × g for 5 min in a swing out 5804 S-4-72 rotor
330 (Eppendorf). Baculovirus infected insect cell (BIIC) stocks were made by infecting SF9 cells

331 with P1 virus and freezing cells before lysis (typically around 36 h) in a 1° cooling rate rack
332 (#NU200 Nalgene) at −80 °C. P1 virus was propagated to passage 2 (P2) by infecting 50 ml
333 of SF9 (VWR, #EM71104-3) culture and harvesting after 5–7 days as described above. For
334 large-scale expression, 500 ml of SF9 cells at a density of 1–1.5 × 106 cells/ml were infected
335 with one vial of BIIC or P2 virus. Cells were harvested when 90% infection rate was achieved
336 as observed by YFP fluorescence, typically between 48 and 72 h. Cells were pelleted at 252
337 × g in a SLA-3000 rotor (Thermo Scientific) for 20 min. The pellet was resuspended in 4 ml of
338 SF9 lysis buffer (50 mM Sodium phosphate pH 7.5, 150 mM NaCl, 20 mM Imidazole, 0.1%
339 Tween 20, 1.5 mM MgCl2) per gram of cell pellet, supplemented with 0.1 mM ATP and
340 cOmplete protease inhibitor cocktail (#05056489001, Roche) and lysed using a douncer
341 (#885301, Kontes) with 20 strokes. Lysates were then cleared by centrifugation at 38,000 × g
342 in a SS-34 rotor (Sorvall) for 30 min, or 200,000 × g for 40 min in a T865 rotor (Sorvall). SP
343 Sepharose beads (#17-0729-01, GE Healthcare) were equilibrated with the lysis buffer and
344 the cleared lysate obtained is mixed with the beads and batch bound for 1 h. Next, the beads
345 were loaded onto a 5 ml disposable polypropylene gravity column (#29922, Thermo Scientific)
346 and washed with at least 10 CV SP wash buffer (50 mM sodium phosphate pH 7.5, 150 mM
347 NaCl) and eluted with SP elution buffer (50 mM sodium phosphate pH 7.5, 300 mM NaCl).
348 The peak fractions obtained were pooled and diluted with Ni-NTA lysis buffer (50 mM sodium
349 phosphate pH 7.5, 150 mM NaCl, 20 mM Imidazole, 10% glycerol) and batch bound to Ni-
350 NTA beads (#30230, Qiagen) for 1 h. The beads were loaded onto a gravity column and
351 washed with at least 10 CV of Ni-NTA wash buffer (50 mM sodium phosphate pH 7.5, 150
352 mM NaCl, 50 mM imidazole and 10% glycerol) and eluted with Ni-NTA elution buffer (50 mM
353 sodium phosphate pH 7.5, 150 mM NaCl, 150 mM Imidazole, 0.1 mM ATP and 10% glycerol).
354 The peak fractions were run on an SDS-PAGE gel for visualisation and protein was aliquoted,
355 flash frozen and stored in liquid nitrogen.
356 Recombinant Kinesin Heavy Chain from *Drosophila melanogaster* was purified as described
357 previously (Coy et al., 1999). Briefly, BL21 DE3 (Invitrogen) were transformed with plasmid
358 pPK113-6H-DHK (accession # AF053733), and the cells were grown at 37 ºC until OD_{600nm}
359 reached 0.5. Expression was induced with 0.4 mM Isopropyl β-D-1-thiogalactopyranoside at
360 15 °C overnight. Cells were harvested by centrifugation (3000 × *g*, 15 min, RT). Cell pellets
361 were stored at -80 °C. For purification, pellets were thawed on ice, and cells were lysed by
362 sonication in buffer A (50 mM phosphate buffer pH 7.5, 300 mM NaCl, 10% glycerol, 1 mM
363 $MgCl_2$, 0.1 mM ATP, and 40 mM Imidazole). The lysate was clarified by centrifugation
364 (100,000 × *g*, T865 rotor, 30 min, 4 °C) and the supernatant was then loaded onto 1 ml HisTrap
365 HP column (Qiagen) at 4 °C. Unbound protein was washed with buffer A containing 90 mM
366 imidazole. Finally, the protein was eluted over 300 mM imidazole gradient (10 column

367 volumes). The peak fractions were run on an SDS-PAGE gel for visualisation and protein was
368 aliquoted, flash frozen and stored in liquid nitrogen.
369
370 **Force measurements**
371 560 nm Polystyrene beads (Polysciences) and motor protein were incubated together in 80
372 mM PIPES pH 7, 2 mM $MgSO_4$, 1 mM EGTA, 1 mM DTT, 3 mg/ml D-Glucose, 0.2 mg/ml
373 casein and 1 mM ATP. The concentration of motor was decreased such that only 20-30% of
374 the beads moved. Flow cell coverslips were plasma-cleaned and functionalized with APTES
375 silane. Two coverslips were stuck together with Dow Corning High Vacuum Grease. Two lines
376 of grease were applied to the base coverslip (22 × 50 mm) using a syringe, the top coverslip
377 (22 × 22 mm) was placed, forming a flow cell of approximately 10 µl capacity. For covalent
378 attachment of microtubules, glutaraldehyde (8%) was added to the flow cell and incubated for
379 30 min. The flow cell was washed with MilliQ water. The microtubules were diluted to the
380 required concentration and introduced to the flow cell and allowed to adsorb onto the surface.
381 The microtubules were incubated for an hour to allow for covalent attachment. Next, 0.2 µl of
382 bead-motor protein solution was diluted in 20 µl of assay buffer composed of BRB80, 1 mM
383 ATP, 0.4 mg/ml casein, 10 µM taxol and 0.4 µl oxygen scavenger mix (1 mg/ml catalase, 5
384 mg/ml Glucose oxidase, 50% glycerol). The beads were then flown to the cell and
385 microtubules were visualised using in-built differential interference contrast on the Optical Trap
386 setup (Carter and Cross, 2005). The trap was steered to position the bead above the
387 microtubule and the image was projected onto the quadrant photodiode detector. Bead
388 positions were acquired at 20 kHz for 180 s, trap stiffness 0.065 to 0.075 pN nm^{-1} for KHC,
389 0.06 to 0.067 pN nm^{-1} for wildtype KIF1C-GFP, 0.01 to 0.052 pN nm^{-1} for KIF1C_{P176L}-GFP and
390 0.014 pN nm^{-1} for KIF1C_{R169W}-GFP. A calibration for trap stiffness was done each day before
391 commencement of measurements. Measurements were done under conditions when 20% or
392 less beads were running on microtubules. Traces with unusual high force events that
393 suggested more than one motor is engaged were excluded from the analysis. For wildtype
394 KIF1C-GFP, data was pooled from 38 recordings of 7 motile beads from 3 independent
395 experiments. For KIF1C_{P176L}-GFP, data pooled from 21 recordings of 6 motile beads from 4
396 independent experiments. For KIF1C_{R169W}-GFP data pooled from 3 recordings of 2 motile
397 beads from 1 experiment. KHC data are a subset of a previously published dataset (Toleikis
398 et al., 2020) with the exception that step analysis only included data acquired at a comparable
399 trap stiffness to KIF1C data and data from superstall conditions were only included for the stall
400 force analysis. Data analysis was carried out using custom code written in R. From the traces
401 generated, a moving window t-test algorithm (Carter and Cross, 2005) was used to identify
402 steps with the following parameters – t-test score threshold=30, minimum step size=5 nm,
403 minimum force=1 pN, moving average, n=20 (1 ms). The size of the window and the threshold

404 are varied to determine accurate steps. When the bead returns to within 20 nm of the centre
405 of the trap, we designated this as a detachment. Other movements towards the trap centre
406 are designated as backslips. The stall force is defined as the force at which the motor
407 undertakes as many forward steps as backslips. We only considered backslips of up to 12
408 nm for the fore/back ratio as their probability of detection is comparable to forward steps.
409 In parallel to single-step analysis, we also carried out a broader run-event analysis. This
410 analysis was used for determining the peak force and duration of force-generation events, and
411 the force-velocity curve. Data was smoothed by 2000-point averaging (100 ms) and events
412 above 0.5 pN force, lasting more than 0.2 s, were included. The end of the run was registered
413 when the event returned below 0.5 pN threshold. Force-velocity relationship was determined
414 from linear fits to the displacement versus time data smoothed by 200 points (10 ms) over 0.5
415 pN force bins.
416
417 **Single molecule motility assays**
418 Microtubules were assembled from 5 µl of 18 mg/ml unlabelled pig tubulin, 0.2 µl of 1 mg/ml
419 HiLyte Fluor 647 or X-rhodamine-labelled tubulin (#TL670M, #TL6290M, Cytoskeleton) and
420 0.5 µl of 0.5 mg/ml biotin tubulin (#T333P, Cytoskeleton) in 15 µl MRB80 (80 mM PIPES pH
421 6.8, 4 mM MgCl2, 1 mM EGTA, 1 mM DTT) supplemented with 4 mM GTP. The mixture was
422 incubated at 37ºC for 90 min before diluting in 80 µl MRB80 supplemented with 20 µM Taxol.
423 Unincorporated tubulin was removed by pelleting microtubules through a glycerol cushion
424 (30% glycerol in MRB80) at 20,238 × g for 12 min at room temperature. The microtubule pellet
425 was resuspended in 80 µl of MRB80 with 20 µM Taxol and stored at 28ºC covered from light
426 for use on the same day.
427 Coverslips (22 × 22) were cleaned by incubating in 2.3 M hydrochloric acid overnight at 60 °C.
428 The next day, coverslips were washed with Millipore water and sonicated at 60 °C for 5 min.
429 The wash cycle was repeated five times. The coverslips were dried using a Spin Clean
430 (Technical video) and plasma cleaned using Henniker plasma clean (HPT-200) for 3 min. Flow
431 chambers were made using clean glass slides (Menzel Gläser Superfrost Plus, Thermo
432 Scientific) and double- sided sticky tape (Scotch 3 M) by placing the cleaned coverslip on the
433 sticky tape creating a 100 µm deep flow chamber. The surface was coated with (0.2 mg/ml)
434 PLL(20)-g[3.5]-PEG(2)/PEG(3.4)-Biotin (50%) (#PLL(20)-g[3.5]-PEG(2)/PEGbi, Susos AG).
435 Biotin-647-microtubules were attached to this surface with streptavidin (0.625 mg/ml) (#S4762
436 Sigma) and the surface was blocked with κ-casein (1 mg/ml) (#C0406 Sigma).
437 KIF1C-GFP, KIF1C$_{P176L}$-GFP and KIF1C$_{R169W}$-GFP were diluted in TIRF Assay Buffer (25 mM
438 HEPES-KOH pH 7.2, 5 mM MgSO4, 1 mM EGTA, 1 mM DTT, 10 µM Taxol) supplemented
439 with 0.05% Tween-20, 25 mM KCl and 200ng/ml κ-casein, spun at 100,000 × g for 10 min in
440 an Airfuge (Beckman Coulter) and fluorescence at 507 nm measured using a NanoDrop™

441 3300 Fluorospectrometer to confirm comparable concentrations are used in the assay.
442 Proteins were then added to the motility mix (TIRF Assay Buffer supplemented with 5 mM
443 ATP, 5 mM phosphocreatine (#P7936, Sigma), 7 U/ml creatine phosphokinase (#C3755
444 Sigma), 0.2 mg/ml catalase, 0.4 mg/ml glucose oxidase, 4 mM DTT, 50 mM glucose (#G8270,
445 Sigma), 25 mM KCl, 10 μM taxol, 0.2 mg/ml κ-casein) and flown into the chamber.
446 Chambers were observed on an Olympus TIRF system using a ×100 NA 1.49 objective, 488
447 and 640 nm laser lines, an ImageEM emCCD camera (Hamamatsu Photonics) under the
448 control of xCellence software (Olympus), an environmental chamber maintained at 25 °C
449 (Okolab, Ottaviano, Italy). Images were acquired at 5 fps for 180 seconds using 2x2 binning,
450 thus the resulting images have 162 nm pixels and 200 ms temporal resolution.
451 Motility was analysed by tracing microtubules and generating maximum intensity kymographs
452 from 7 pixel wide lines using the ImageJ Kymograph plugin from Arne Seitz (EPFL Lausanne).
453 Motor tracks from kymographs were traced by hand and recorded as ImageJ ROIs. These
454 paths were analysed in a custom-built python analysis script. Individual phases of tracks were
455 segmented from the ROI, and motors were said to be translocating towards the plus-end or
456 minus-end of the microtubule in each phase if their speed towards that end of the microtubule
457 was greater than 25 nm/s. When the motor's speed was less than 25 nm/s, it was annotated
458 as paused. Motors with an average speed of less than 25 nm/s or a total run length of less
459 than 500 nm were considered as static. Non-static motors that underwent bidirectional motion
460 of at least 324 nm or just moved towards the minus end where classed as diffusing. Only the
461 remaining, plus end directed motors were analysed for run parameters. Dwell times were
462 calculated as the total time the motor spent on the microtubule until it reaches the plus end or
463 the end of the recording. Run length is the total distance covered by the motor. The average
464 speed was calculated as the run length divided by the dwell time. The pause-corrected
465 average speed was also calculated by dividing the run length by the dwell time minus any time
466 when the motor was paused. Superplots show the mean speed, run-length, or dwell time for
467 a given experimental day, with smaller colour-coded spots showing the individual measured
468 values of motors. On each of the three experiment days, one to four chambers were prepared
469 for each protein. Statistics were calculated at the per-motor level between experimental
470 groups. The data were tested for normality using D'Agostino and Pearson's test, and as they
471 were not normally distributed, a Kruskal-Wallis test was used to determine if experimental
472 groups differed significantly. Where a statistically significant difference was indicated, pairwise
473 interactions were tested using Conover's post-hoc test and p-values were corrected for
474 multiple comparisons using the Holm-Bonferroni method.
475
476 **KIF1C localisation and mitochondria transport assays**

477 pKIF1C$_{P176L}$-GFP and pKIF1C$_{R169W}$-GFP were based on pKIF1C$_{RIP2}$-GFP (available from
478 Addgene 130977 (Efimova et al., 2014). R169W was introduced using a mutagenesis PCR
479 with upstream primer UT01 (5'-GGAATTCTGGAGCTATGGCTGGTG-3'), mutagenesis
480 primer AS376 (5'-CTGCGGGTC**T**GGGAGCACC-3') and downstream primer UT170 (5'-
481 ACTGACCTTCTCCGAGTCC-3'). The fragment containing the mutation was replaced in
482 pKIF1C$_{RIP2}$-GFP using *Eco*RI and *Bsi*WI. P176L was introduced using a mutagenesis PCR
483 with upstream primer UT01, mutagenesis primer AS528 (5'-
484 CTGCACGTAC**A**GGCCCAGGATG-3') and downstream primer AS359 (5'-
485 GGGGATCCCCTCGTTCCCGTTCC-3'). The fragment containing the mutation was replaced
486 in pKIF1C$_{RIP2}$-GFP using *Eco*RI and *Bsp*EI.
487 pKIF1C-mCherry-FRB, pKIF1C$_{P176L}$-mCherry-FRB and pKIF1C$_{R169W}$-mCherry-FRB plasmids
488 were based on pβactin-KIF1C_MD-GFP-FRB, a kind gift from Caspar Hoogenraad (Lipka et
489 al., 2016) .The KIF1C motor domain was replaced with full length human KIF1C fused to
490 mCherry from pKIF1C-mCherry (available from Addgene 130978 (Theisen et al., 2012)) using
491 *Nhe*I and *Bsr*GI. The mutations were introduced from pKIF1C$_{P176L}$-GFP and pKIF1C$_{R169W}$-GFP
492 using *Nhe*I and *Bam*HI. FKBP-GFP-Myc-MAO was a kind gift from Sean Munro (MRC-LMB,
493 Cambridge) (Wong and Munro, 2014).
494 hTERT RPE1 cells (ATCC) were grown in DMEM/Nutrient F-12 Ham (#D6421 Sigma)
495 supplemented with 10% FBS (Sigma), 2 mM L-glutamine (Sigma), 100 U/ml penicillin (Sigma),
496 100 µg/ml streptomycin (Sigma) and 2.3 g/l sodium bicarbonate (#S8761 Sigma) in a
497 humidified incubator at 37ºC and 8% CO_2.
498 For tail localisation experiments, RPE1 cells were co-transfected with 0.75 µg KIF1C-mCherry
499 and 0.75 µg of either KIF1C-GFP, pKIF1C$_{P176L}$-GFP or pKIF1C$_{R169W}$-GFP using Fugene 6
500 (Promega) in fibronectin-coated glass-bottom dishes and imaged 24 hours later on an
501 Olympus Deltavision microscope (Applied Precision, LLC) equipped with eGFP, mCherry filter
502 sets and a CoolSNAP HQ2 camera (Roper Scientific) under the control of SoftWorx (Applied
503 Precision). 37ºC and 5% CO_2 were maintained in a TOKAI Hit stage incubator. Images from
504 migrating cells with a tail at the rear expressing moderate levels of both markers were acquired
505 in both channels. To determine tail accumulation, average intensity measurements from the
506 perinuclear area, the tip of cell tails and background outside of the cell were taken for both
507 channels. After background subtraction, the ratio of tail versus cytoplasm intensity was
508 calculated for both channels. The ratio of GFP versus mCherry channel was calculated as the
509 relative enrichment of the protein of interest versus wildtype KIF1C-mCherry. 3 experiments
510 with a total of 69-77 cells were analysed for each condition.
511 For mitochondria transport experiments, RPE1 cells were co-transfected with 1 µg KIF1C-
512 mCherry-FRB and 0.5 µg FKBP-GFP-Myc-MAO using Fugene 6 (Promega) in fibronectin-
513 coated glass-bottom dishes and imaged 24 hours later on an Olympus Deltavision microscope

514 (Applied Precision, LLC) equipped with eGFP, mCherry filter sets and a CoolSNAP HQ2
515 camera (Roper Scientific) under the control of SoftWorx (Applied Precision). Live cells were
516 imaged using an Olympus 40x UPlanFL N Oil NA1.3 objective in imaging medium (Leibovitz's
517 L-15 medium (Gibco™ 21083027) without phenol red, supplemented with 10% FBS (Sigma),
518 2 mM L-glutamine (Sigma), 100 U/ml penicillin (Sigma), 100 µg/ml streptomycin (Sigma)) at
519 37 °C. Cells expressing moderate levels of both KIF1C and the mitochondrial marker were
520 identified and their stage position labelled. Images in both channels were acquired from each
521 stage position at 2-minute intervals for 22 minutes to determine organelle redistribution. After
522 the first image from each cell, rapamycin was added to the imaging dish at a final concentration
523 of 200 µM. To observe mitochondria morphology change and motility, images from a single
524 cell were acquired at 2 s intervals for 10 minutes and rapamycin added after 30 seconds.
525 To quantify organelle redistribution, 33 pixel wide line profiles were acquired from the cell
526 centre to the cell tips at each timepoint. The average intensity of the KIF1C signal along the
527 entire line was used to include only cells with comparable expression level across the wildtype
528 and mutant constructs. Positions along line profiles were normalised so that the cell centre
529 was set to 0 and the cell tip to 1. This normalised distance was binned into 100 equal-width
530 bins and intensity values of MAO for each cell were sorted into these bins. The centre of each
531 bin was plotted against the average MAO intensity +/- the standard error of the binned values.
532 To quantify mitochondria redistribution over time, periphery GFP-MOA signal (0.8 to 1.0) was
533 divided by perinuclear GFP-MOA signal (0.0 to 0.2).
534

535 **Acknowledgements**

536 The authors gratefully acknowledge Nicholas Carter and CAMDU (Computing and Advanced
537 Microscopy Unit) for access to the optical trap and microscopy support and Alice Bachmann
538 for generating KIF1C$_{R169W}$-GFP.
539 This work was funded by a Research Prize from the Lister Institute of Preventive Medicine
540 and a Wellcome Trust Investigator Award (200870/Z/16/Z) to A.S., a Lister Institute Summer
541 Studentship and a Chancellor's International PhD Scholarship from the University of Warwick
542 that supported N.S., and a Ph.D. studentship from the MRC Doctoral Training Partnership
543 (MR/N014294/1) that supported A.J.Z. D.R. is supported in part from the University of
544 Warwick. A.T. and R.C were supported by a Wellcome Senior Investigator Award
545 (103895/Z/14/Z).
546

547 **Author Contributions**

548 A.S. and N.S. conceived the project. N.S. cloned and purified KIF1C wt and mutants and
549 performed tail localisation experiments. D.R. cloned mammalian expression constructs,
550 performed single molecule experiments & analysed data. A.T. and N.S. performed Kif1C

551 optical trapping experiments and analysed the data. A.T. purified KHC, performed KHC optical
552 trapping experiments and analysed the data. A.S. performed cellular transport assays. A.Z.
553 analysed single molecule motility and cellular transport data. AS wrote the manuscript with
554 contributions from all authors.
555
556 **Bibliography**

557 BLOCK, S. M., GOLDSTEIN, L. S. & SCHNAPP, B. J. 1990. Bead movement by
558 single kinesin molecules studied with optical tweezers. *Nature,* 348**,** 348-352.
559 BOUSLAM, N., BOUHOUCHE, A., BENOMAR, A., HANEIN, S., KLEBE, S.,
560 AZZEDINE, H., DI GIANDOMENICO, S., BOLAND-AUGE, A., SANTORELLI,
561 F. M., DURR, A., BRICE, A., YAHYAOUI, M. & STEVANIN, G. 2007. A novel
562 locus for autosomal recessive spastic ataxia on chromosome 17p. *Hum*
563 *Genet,* 121**,** 413-20.
564 BOYLE, L., RAO, L., KAUR, S., FAN, X., MEBANE, C., HAMM, L., THORNTON, A.,
565 AHRENDSEN, J. T., ANDERSON, M. P. & CHRISTODOULOU, J. 2021.
566 Genotype and defects in microtubule-based motility correlate with clinical
567 severity in KIF1A-associated neurological disorder. *Human Genetics and*
568 *Genomics Advances,* 2**,** 100026.
569 BUDAITIS, B. G., JARIWALA, S., RAO, L., YUE, Y., SEPT, D., VERHEY, K. J. &
570 GENNERICH, A. 2021. Pathogenic mutations in the kinesin-3 motor KIF1A
571 diminish force generation and movement through allosteric mechanisms.
572 *Journal of Cell Biology,* 220.
573 CABALLERO OTEYZA, A., BATTALOGLU, E., OCEK, L., LINDIG, T.,
574 REICHBAUER, J., REBELO, A. P., GONZALEZ, M. A., ZORLU, Y., OZES, B.,
575 TIMMANN, D., BENDER, B., WOEHLKE, G., ZUCHNER, S., SCHOLS, L. &
576 SCHULE, R. 2014. Motor protein mutations cause a new form of hereditary
577 spastic paraplegia. *Neurology,* 82**,** 2007-16.
578 CARTER, N. J. & CROSS, R. A. 2005. Mechanics of the kinesin step. *Nature,* 435**,**
579 308-12.
580 COY, D. L., WAGENBACH, M. & HOWARD, J. 1999. Kinesin takes one 8-nm step
581 for each ATP that it hydrolyzes. *Journal of Biological Chemistry,* 274**,** 3667-
582 3671.
583 DOR, T., CINNAMON, Y., RAYMOND, L., SHAAG, A., BOUSLAM, N.,
584 BOUHOUCHE, A., GAUSSEN, M., MEYER, V., DURR, A., BRICE, A.,

585 BENOMAR, A., STEVANIN, G., SCHUELKE, M. & EDVARDSON, S. 2014.
586 KIF1C mutations in two families with hereditary spastic paraparesis and
587 cerebellar dysfunction. *J Med Genet,* 51**,** 137-42.
588 DORNER, C., CIOSSEK, T., MULLER, S., MOLLER, P. H., ULLRICH, A. &
589 LAMMERS, R. 1998. Characterization of KIF1C, a new kinesin-like protein
590 involved in vesicle transport from the Golgi apparatus to the endoplasmic
591 reticulum. *J Biol Chem,* 273**,** 20267-75.
592 EFIMOVA, N., GRIMALDI, A., BACHMANN, A., FRYE, K., ZHU, X., FEOKTISTOV,
593 A., STRAUBE, A. & KAVERINA, I. 2014. Podosome-regulating kinesin KIF1C
594 translocates to the cell periphery in a CLASP-dependent manner. *J Cell Sci,*
595 127**,** 5179-88.
596 FRIEDMAN, D. S. & VALE, R. D. 1999. Single-molecule analysis of kinesin motility
597 reveals regulation by the cargo-binding tail domain. *Nature cell biology,* 1**,**
598 293-297.
599 GABRYCH, D. R., LAU, V. Z., NIWA, S. & SILVERMAN, M. A. 2019. Going Too Far
600 Is the Same as Falling Short(dagger): Kinesin-3 Family Members in
601 Hereditary Spastic Paraplegia. *Front Cell Neurosci,* 13**,** 419.
602 HEDERA, P., ELDEVIK, O. P., MALY, P., RAINIER, S. & FINK, J. K. 2005. Spinal
603 cord magnetic resonance imaging in autosomal dominant hereditary spastic
604 paraplegia. *Neuroradiology,* 47**,** 730-4.
605 KAAN, H. Y. K., HACKNEY, D. D. & KOZIELSKI, F. 2011. The structure of the
606 kinesin-1 motor-tail complex reveals the mechanism of autoinhibition.
607 *Science,* 333**,** 883-885.
608 KENDRICK, A. A., DICKEY, A. M., REDWINE, W. B., TRAN, P. T., VAITES, L. P.,
609 DZIECIATKOWSKA, M., HARPER, J. W. & RECK-PETERSON, S. L. 2019.
610 Hook3 is a scaffold for the opposite-polarity microtubule-based motors
611 cytoplasmic dynein-1 and KIF1C. *J Cell Biol*.
612 KHALIL, A. S., APPLEYARD, D. C., LABNO, A. K., GEORGES, A., KARPLUS, M.,
613 BELCHER, A. M., HWANG, W. & LANG, M. J. 2008. Kinesin's cover-neck
614 bundle folds forward to generate force. *Proceedings of the National Academy*
615 *of Sciences,* 105**,** 19247-19252.
616 KLEBE, S., LOSSOS, A., AZZEDINE, H., MUNDWILLER, E., SHEFFER, R.,
617 GAUSSEN, M., MARELLI, C., NAWARA, M., CARPENTIER, W., MEYER, V.,
618 RASTETTER, A., MARTIN, E., BOUTEILLER, D., ORLANDO, L., GYAPAY,

619 G., EL-HACHIMI, K. H., ZIMMERMAN, B., GAMLIEL, M., MISK, A., LERER,
620 I., BRICE, A., DURR, A. & STEVANIN, G. 2012. KIF1A missense mutations in
621 SPG30, an autosomal recessive spastic paraplegia: distinct phenotypes
622 according to the nature of the mutations. *Eur J Hum Genet,* 20**,** 645-9.
623 LAM, A. J., RAO, L., ANAZAWA, Y., OKADA, K., CHIBA, K., DACY, M., NIWA, S.,
624 GENNERICH, A., NOWAKOWSKI, D. W. & MCKENNEY, R. J. 2021. A highly
625 conserved 310 helix within the kinesin motor domain is critical for kinesin
626 function and human health. *Science advances,* 7**,** eabf1002.
627 LEE, P. L., OHLSON, M. B. & PFEFFER, S. R. 2015. Rab6 regulation of the kinesin
628 family KIF1C motor domain contributes to Golgi tethering. *Elife,* 4.
629 LIPKA, J., KAPITEIN, L. C., JAWORSKI, J. & HOOGENRAAD, C. C. 2016.
630 Microtubule-binding protein doublecortin-like kinase 1 (DCLK1) guides
631 kinesin-3-mediated cargo transport to dendrites. *EMBO J,* 35**,** 302-18.
632 MARCHIONNI, E., MENERET, A., KEREN, B., MELKI, J., DENIER, C., DURR, A.,
633 APARTIS, E., BOESPFLUG-TANGUY, O. & MOCHEL, F. 2019. KIF1C
634 Variants Are Associated with Hypomyelination, Ataxia, Tremor, and Dystonia
635 in Fraternal Twins. *Tremor Other Hyperkinet Mov (N Y),* 9.
636 NANGAKU, M., SATO-YOSHITAKE, R., OKADA, Y., NODA, Y., TAKEMURA, R.,
637 YAMAZAKI, H. & HIROKAWA, N. 1994. KIF1B, a novel microtubule plus end-
638 directed monomeric motor protein for transport of mitochondria. *Cell,* 79**,**
639 1209-20.
640 NOVARINO, G., FENSTERMAKER, A. G., ZAKI, M. S., HOFREE, M., SILHAVY, J.
641 L., HEIBERG, A. D., ABDELLATEEF, M., ROSTI, B., SCOTT, E., MANSOUR,
642 L., MASRI, A., KAYSERILI, H., AL-AAMA, J. Y., ABDEL-SALAM, G. M. H.,
643 KARMINEJAD, A., KARA, M., KARA, B., BOZORGMEHRI, B., BEN-OMRAN,
644 T., MOJAHEDI, F., EL DIN MAHMOUD, I. G., BOUSLAM, N., BOUHOUCHE,
645 A., BENOMAR, A., HANEIN, S., RAYMOND, L., FORLANI, S., MASCARO,
646 M., SELIM, L., SHEHATA, N., AL-ALLAWI, N., BINDU, P. S., AZAM, M.,
647 GUNEL, M., CAGLAYAN, A., BILGUVAR, K., TOLUN, A., ISSA, M. Y.,
648 SCHROTH, J., SPENCER, E. G., ROSTI, R. O., AKIZU, N., VAUX, K. K.,
649 JOHANSEN, A., KOH, A. A., MEGAHED, H., DURR, A., BRICE, A.,
650 STEVANIN, G., GABRIEL, S. B., IDEKER, T. & GLEESON, J. G. 2014.
651 Exome sequencing links corticospinal motor neuron disease to common
652 neurodegenerative disorders. *Science,* 343**,** 506-511.

653 OKADA, Y., HIGUCHI, H. & HIROKAWA, N. 2003. Processivity of the single-headed
654 kinesin KIF1A through biased binding to tubulin. *Nature,* 424**,** 574-7.
655 OKADA, Y. & HIROKAWA, N. 1999. A processive single-headed motor: kinesin
656 superfamily protein KIF1A. *Science,* 283**,** 1152-7.
657 OKADA, Y., YAMAZAKI, H., SEKINE-AIZAWA, Y. & HIROKAWA, N. 1995. The
658 neuron-specific kinesin superfamily protein KIF1A is a unique monomeric
659 motor for anterograde axonal transport of synaptic vesicle precursors. *Cell,*
660 81**,** 769-80.
661 PASCHAL, B. M. & VALLEE, R. B. 1987. Retrograde transport by the microtubule-
662 associated protein MAP 1C. *Nature,* 330**,** 181-183.
663 RAY, S., MEYHÖFER, E., MILLIGAN, R. A. & HOWARD, J. 1993. Kinesin follows
664 the microtubule's protofilament axis. *The Journal of cell biology,* 121**,** 1083-
665 1093.
666 REID, E., KLOOS, M., ASHLEY-KOCH, A., HUGHES, L., BEVAN, S., SVENSON, I.
667 K., GRAHAM, F. L., GASKELL, P. C., DEARLOVE, A. & PERICAK-VANCE,
668 M. A. 2002. A kinesin heavy chain (KIF5A) mutation in hereditary spastic
669 paraplegia (SPG10). *The American Journal of Human Genetics,* 71**,** 1189-
670 1194.
671 ROGERS, K. R., WEISS, S., CREVEL, I., BROPHY, P. J., GEEVES, M. & CROSS,
672 R. 2001. KIF1D is a fast non-processive kinesin that demonstrates novel K-
673 loop-dependent mechanochemistry. *EMBO J,* 20**,** 5101-13.
674 SCARABELLI, G., SOPPINA, V., YAO, X.-Q., ATHERTON, J., MOORES,
675 CAROLYN A., VERHEY, KRISTEN J. & GRANT, BARRY J. 2015. Mapping
676 the Processivity Determinants of the Kinesin-3 Motor Domain. *Biophysical*
677 *Journal,* 109**,** 1537-1540.
678 SCHLAGER, M. A., KAPITEIN, L. C., GRIGORIEV, I., BURZYNSKI, G. M., WULF,
679 P. S., KEIJZER, N., DE GRAAFF, E., FUKUDA, M., SHEPHERD, I. T.,
680 AKHMANOVA, A. & HOOGENRAAD, C. C. 2010. Pericentrosomal targeting
681 of Rab6 secretory vesicles by Bicaudal-D-related protein 1 (BICDR-1)
682 regulates neuritogenesis. *EMBO J,* 29**,** 1637-51.
683 SCHULE, R., WIETHOFF, S., MARTUS, P., KARLE, K. N., OTTO, S., KLEBE, S.,
684 KLIMPE, S., GALLENMULLER, C., KURZWELLY, D., HENKEL, D.,
685 RIMMELE, F., STOLZE, H., KOHL, Z., KASSUBEK, J., KLOCKGETHER, T.,
686 VIELHABER, S., KAMM, C., KLOPSTOCK, T., BAUER, P., ZUCHNER, S.,

687 LIEPELT-SCARFONE, I. & SCHOLS, L. 2016. Hereditary spastic paraplegia:
688 Clinicogenetic lessons from 608 patients. *Ann Neurol,* 79**,** 646-58.
689 SIDDIQUI, N., ZWETSLOOT, A. J., BACHMANN, A., ROTH, D., HUSSAIN, H.,
690 BRANDT, J., KAVERINA, I. & STRAUBE, A. 2019. PTPN21 and Hook3
691 relieve KIF1C autoinhibition and activate intracellular transport. *Nat Commun,*
692 10**,** 2693.
693 SOPPINA, V., NORRIS, S. R., DIZAJI, A. S., KORTUS, M., VEATCH, S.,
694 PECKHAM, M. & VERHEY, K. J. 2014. Dimerization of mammalian kinesin-3
695 motors results in superprocessive motion. *Proc Natl Acad Sci U S A,* 111**,**
696 5562-7.
697 SVOBODA, K., SCHMIDT, C. F., SCHNAPP, B. J. & BLOCK, S. M. 1993. Direct
698 observation of kinesin stepping by optical trapping interferometry. *Nature,*
699 365**,** 721-727.
700 THEISEN, U., STRAUBE, E. & STRAUBE, A. 2012. Directional persistence of
701 migrating cells requires Kif1C-mediated stabilization of trailing adhesions. *Dev*
702 *Cell,* 23**,** 1153-66.
703 TOLEIKIS, A., CARTER, N. J. & CROSS, R. A. 2020. Backstepping Mechanism of
704 Kinesin-1. *Biophysical Journal,* 119**,** 1984-1994.
705 TOMISHIGE, M., KLOPFENSTEIN, D. R. & VALE, R. D. 2002. Conversion of
706 Unc104/KIF1A kinesin into a processive motor after dimerization. *Science,*
707 297**,** 2263-7.
708 TROWITZSCH, S., BIENIOSSEK, C., NIE, Y., GARZONI, F. & BERGER, I. 2010.
709 New baculovirus expression tools for recombinant protein complex
710 production. *Journal of structural biology,* 172**,** 45-54.
711 WOEHLKE, G., RUBY, A. K., HART, C. L., LY, B., HOM-BOOHER, N. & VALE, R.
712 D. 1997. Microtubule interaction site of the kinesin motor. *Cell,* 90**,** 207-16.
713 WONG, M. & MUNRO, S. 2014. The specificity of vesicle traffic to the Golgi is
714 encoded in the golgin coiled-coil proteins. *Science,* 346.
715 YAMADA, K. H., HANADA, T. & CHISHTI, A. H. 2007. The effector domain of human
716 Dlg tumor suppressor acts as a switch that relieves autoinhibition of kinesin-3
717 motor GAKIN/KIF13B. *Biochemistry,* 46**,** 10039-45.
718 YILDIZ, A., TOMISHIGE, M., GENNERICH, A. & VALE, R. D. 2008. Intramolecular
719 strain coordinates kinesin stepping behavior along microtubules. *Cell,* 134**,**
720 1030-1041.

YUCEL-YILMAZ, D., YUCESAN, E., YALNIZOGLU, D., OGUZ, K. K., SAGIROGLU, M. S., OZBEK, U., SERDAROGLU, E., BILGIC, B., ERDEM, S., ISERI, S. A. U., HANAGASI, H., GURVIT, H., OZGUL, R. K. & DURSUN, A. 2018. Clinical phenotype of hereditary spastic paraplegia due to KIF1C gene mutations across life span. *Brain Dev,* 40**,** 458-464.

729 **FIGURES AND FIGURE LEGENDS**

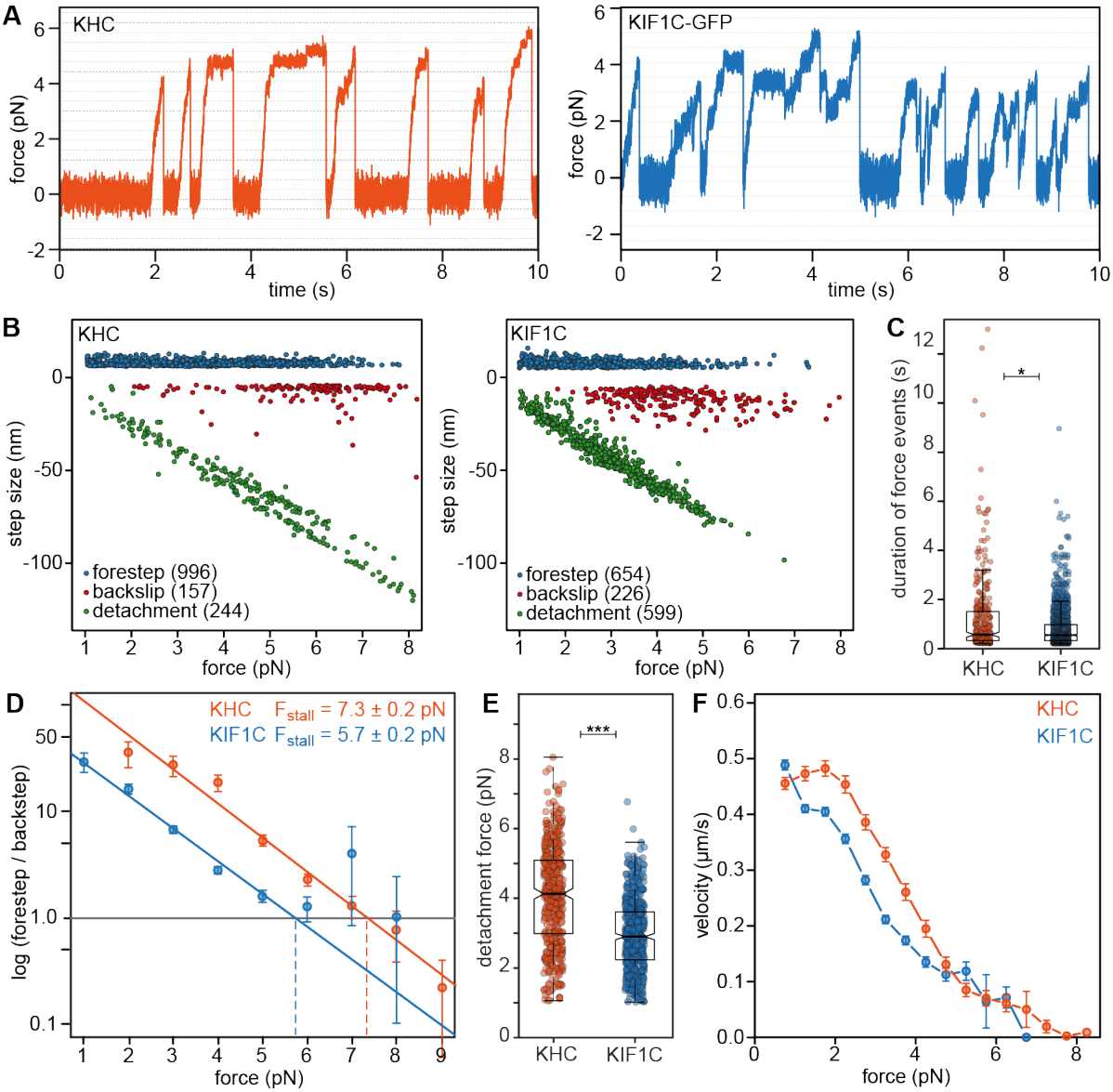

730

731 **Figure 1: KIF1C single molecule force generation. (A)** Representative traces from single
732 bead optical trapping experiment for Drosophila melanogaster kinesin heavy chain (KHC)
733 and human KIF1C. Dotted lines indicate 8 nm displacement. **(B)** Step sizes extracted from
734 single molecule force recordings of KHC and KIF1C plotted relative to the force at which
735 they originated. Number of events for each category are given in brackets. **(C)** Duration over
736 which a force of at least 0.5 pN was maintained. n=333 for KHC and 1378 for KIF1C. *
737 p=0.016 (Wilcoxon rank sum test). **(D)** Forestep to backslip ratio relative to force shows 5.7
738 ± 0.2 pN stall force for KIF1C and 7.3 ± 0.2 pN stall force for KHC. Note that superstall
739 events obtained under added resistive loads are only included in the KHC dataset. **(E)**
740 Distribution of detachment forces. n=460 for KHC and 599 for KIF1C. *** p<0.0001 (t-test).
741 **(F)** Force-velocity relationship for KHC (n=353 individual runs) and KIF1C (n=1662).
742

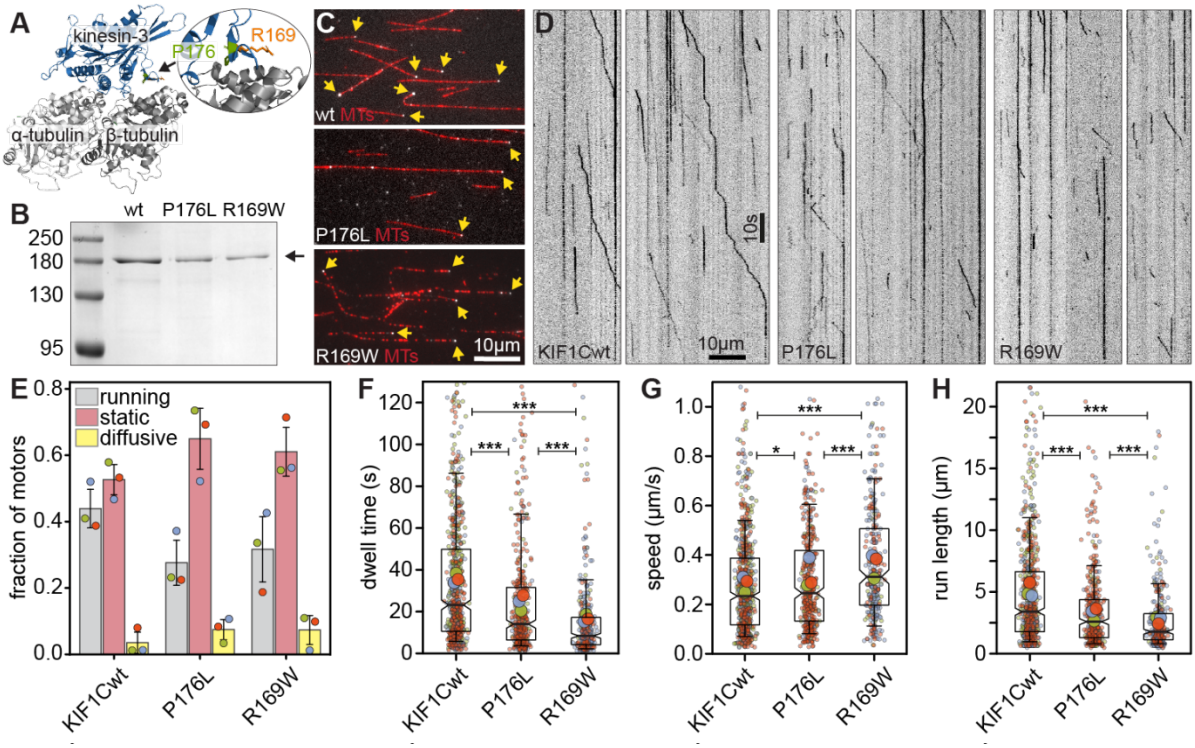

Figure 2: Pathogenic mutations in KIF1C increase unbinding rate and speed. (A) Structure of a kinesin-3 motor domain (blue) bound to a microtubule (grey) with the residues R169 and P176 highlighted. Structure is of related motor KIF1A (PDB reference 4UXP) in which both residues are conserved. **(B)** SDS PAGE analysis of purified recombinant human KIF1C-GFP wildtype, KIF1C$_{P176L}$-GFP and KIF1C$_{R169W}$-GFP and molecular size markers as indicated. **(C)** TIRF micrograph of Taxol-stabilised microtubules (red) and full-length recombinant human KIF1C tagged with GFP (wildtype or carrying mutations as indicated) in greyscale. Plus end accumulation is indicated with yellow arrows. **(D)** Representative kymographs showing motility of KIF1C-GFP wildtype and pathogenic mutants P176L and R169W. **(E)** Fraction of motors that run towards the plus end, are static or diffusive. Bars show mean ± SD of 3 experiments. Coloured dots indicate individual values for each experiment. **(F-H)** Superplots for dwell time, speed and run length of individual motors (small dots), averages per experiment day (large dots) are shown colour-coded by experiment day. Boxes indicate quartiles and whiskers at 10/90%. Note that values outside of the Y axis limits have been omitted, but are included in the statistics. * $p<0.05$; *** $p<0.0001$ (Kruskal Wallis, Conover's test post hoc with Holm correction).

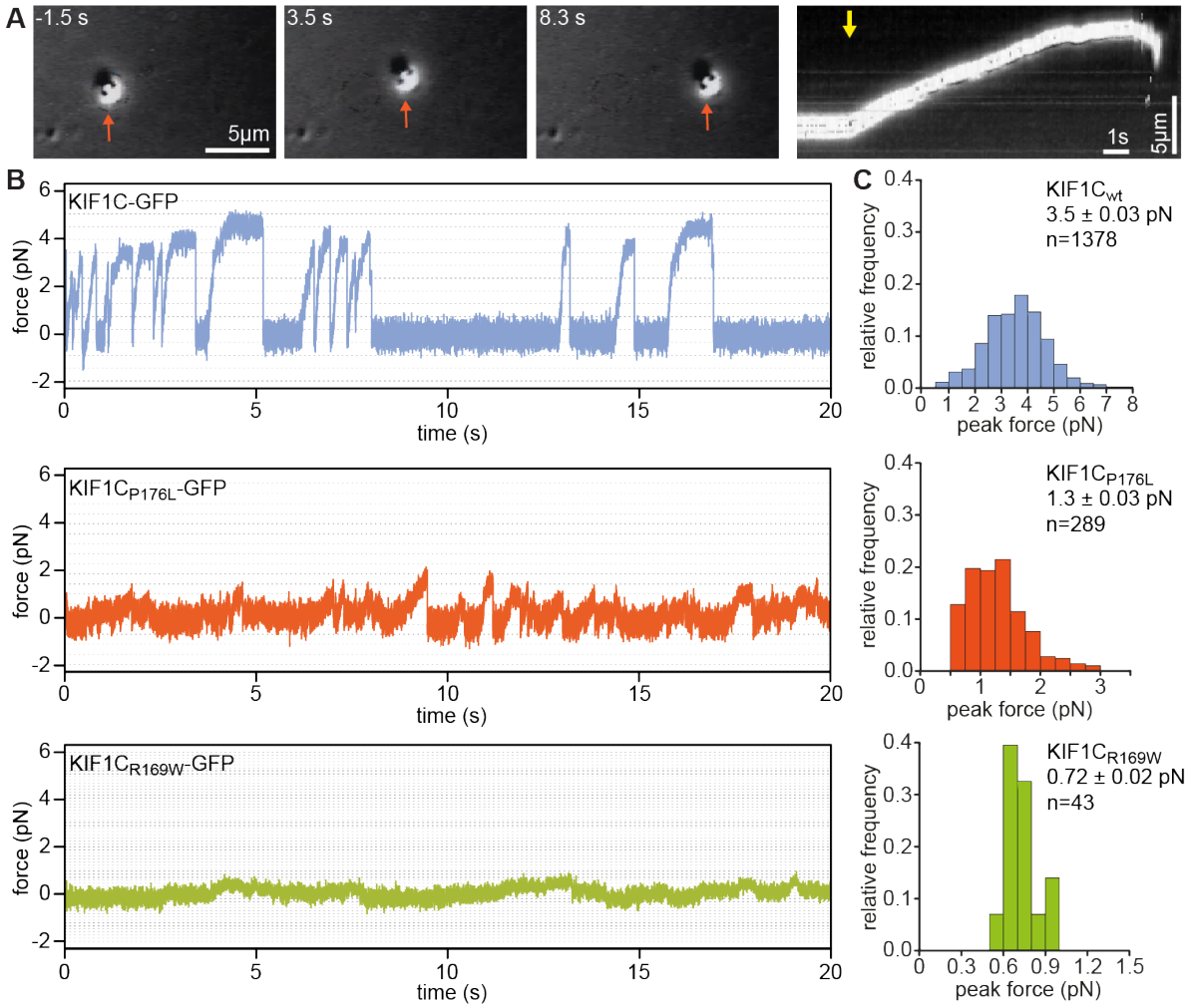

Figure 3: Pathogenic mutations of KIF1C impair force generation. (A) Stills and kymograph from an optical trapping experiment showing processive bead transport by KIF1C$_{P176L}$-GFP after release of the motor from the trap (bead indicated with orange arrow in stills, indicated time relative to trap release indicated by yellow arrow in kymograph). **(B)** Representative traces from optical trapping experiment with KIF1C-GFP wildtype and pathogenic mutants P176L and R169W. Dashed lines indicate 8 nm displacement intervals, which are narrower at low trap stiffness used for mutants. **(C)** Histograms of peak forces determined for event lasting longer than 200 ms that exceed 0.5 pN. Mean ± SEM and number of events are indicated. Groups are significantly different with $p<0.0001$ (Kruskal Wallis, with Sidak correction).

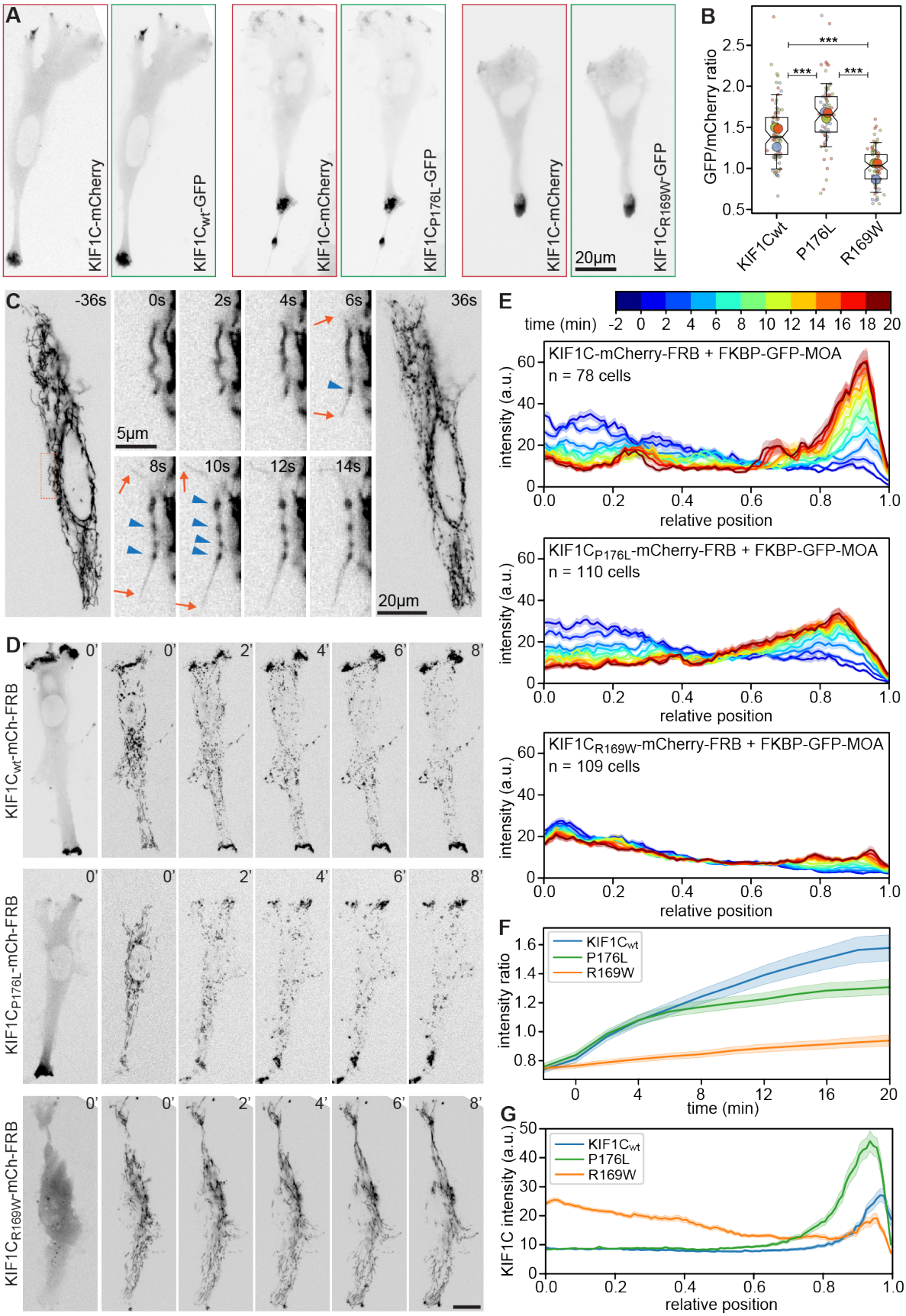

773

774 **Figure 4: Pathogenic mutations of KIF1C impair intracellular cargo transport. (A)** RPE1

775 cells co-expressing KIF1C-mCherry and either wildtype KIF1C-GFP, KIF1C$_{P176L}$-GFP or

776 KIF1C$_{R169W}$-GFP. All proteins accumulate in the tip of cell tails if overexpressed. **(B)** Superplot
777 of 3 cell tail accumulation experiments showing ratio of enrichment in cell tails versus
778 perinuclear cytoplasm for GFP and mCherry constructs. Small circles represent one cell and
779 large circles mean for experiment. Box plots show quartiles and 10/90% whiskers of pooled
780 data. *** p<0.0001 (Kruskal Wallis, Conover's test post hoc with Holm correction). **(C)**
781 Mitochondria morphology changes upon KIF1C recruitment in RPE1 cell expressing KIF1C-
782 mCherry-FRB and FKBP-GFP-MOA. GFP channel shown, indicated times relative to
783 rapamycin addition. Orange box indicates location of zoomed region. Orange arrows indicate
784 membrane tubules pulled out, blue arrowheads indicate beads formed. **(D)** RPE1 cell co-
785 expressing FKBP-GFP-MOA and either wildtype KIF1C-mCherry-FRB, KIF1C$_{P176L}$- mCherry-
786 FRB or KIF1C$_{R169W}$- mCherry-FRB. Left panel shows KIF1C signal, other panels MOA-labelled
787 mitochondria. Time from rapamycin addition indicated in minutes. Scale bar 20µm. **(E)**
788 Averaged linescans showing mitochondria redistribution upon recruitment of wildtype KIF1C,
789 P176L or R169W mutant. Cell position normalised to 0 in cell centre and 1 at cell periphery.
790 Errors show SEM. Time colour-coded as indicated. **(F)** Ratio of GFP-MOA intensity at the cell
791 periphery versus perinuclear area over time. Errors show SEM. **(G)** Averaged linescans
792 showing KIF1C recruitment and KIF1C distribution before rapamycin addition in the same cells
793 analysed for mitochondria redistribution. Cell position normalised to 0 in cell centre and 1 at
794 cell periphery. Errors show SEM.
795
796 **Supplementary Figures**
797

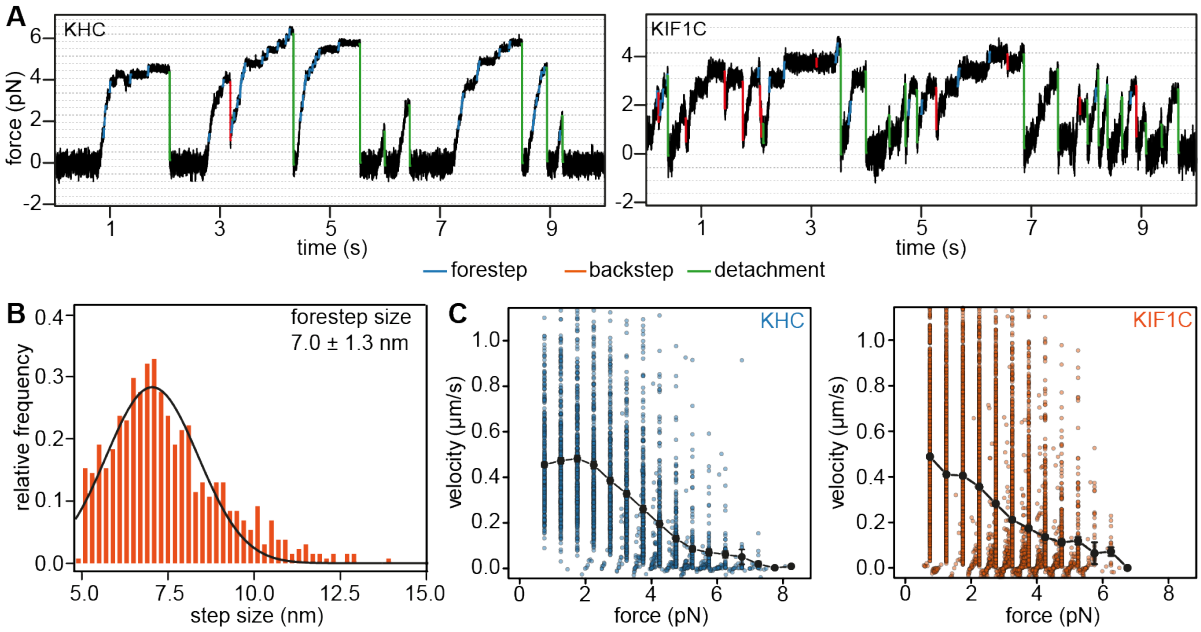

798
799 **Figure S1: Step and force-velocity analysis. (A)** Representative traces from single bead
800 optical trapping experiment for Drosophila melanogaster kinesin heavy chain (KHC) and

human KIF1C. Dotted lines indicate 8 nm displacements. The steps detected using the step-finder are highlighted. Forward steps in blue, backslips in red and detachments in green. Parameters used in step finder algorithm are t-test score threshold=30, minimum step size=5 nm, minimum force=1 pN, moving average=20 (1 ms). **(B)** Forward step-size distribution for KIF1C. Gaussian curve fit with μ = 7.0 nm, σ= 1.3 nm, n=647. **(C)** Distribution of velocity of KHC and KIF1C relative to force (n=353 and n=1662, respectively.)

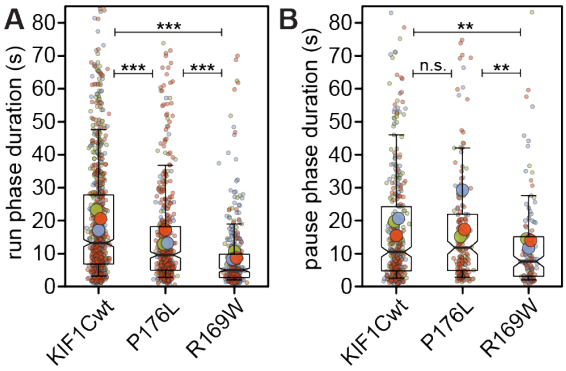

Figure S2: Phase durations from single molecule motility assays. (A-B) Superplots for phase durations for plus end-directed runs (A) and pauses (B) of individual motors (small dots), averages per experiment day (large dots) are shown colour-coded by experiment day. Boxes indicate quartiles and whiskers at 10/90%. Note that values outside of the Y axis limits have been omitted, but are included in the statistics. n.s. p>0.5; ** p<0.005; *** p<0.0001 (Kruskal Wallis, Conover's test post hoc with Holm correction).